

Caustics and velocity caustics in the diffuse interstellar medium at high Galactic latitudes

P. M. W. Kalberla

Argelander-Institut für Astronomie, University of Bonn, Auf dem Hügel 71, 53121 Bonn, Germany
e-mail: pkalberla@astro.uni-bonn.de

Received 25 September 2023 / Accepted 8 December 2023

ABSTRACT

Context. The far-infrared (FIR) distribution at high Galactic latitudes, observed with *Planck*, is filamentary with coherent structures in polarization. These structures are also closely related to H I filaments with coherent velocity structures. There is a long-standing debate about the physical nature of these structures. They are considered either as velocity caustics, fluctuations engraved by the turbulent velocity field or as cold three-dimensional density structures in the interstellar medium (ISM).

Aims. We discuss different approaches to data analysis and interpretation in order to work out the differences.

Methods. We considered mathematical preliminaries for the derivation of caustics that characterize filamentary structures in the ISM. Using the Hessian operator, we traced individual FIR filamentary structures in H I from channel maps as observed and alternatively from data that are provided by the velocity decomposition algorithm (VDA). VDA is claimed to separate velocity caustics from density effects.

Results. Based on the strict mathematical definition, the so-called velocity caustics are not actually caustics. These VDA data products may contain caustics in the same way as the original H I observations. Caustics derived by a Hessian analysis of both databases are nearly identical with a correlation coefficient of 98%. However, the VDA algorithm leads to a 30% increase in the alignment uncertainties when fitting FIR/H I orientation angles. Thus, the VDA velocity crowding concept fails to explain the alignment of FIR/H I filaments at $|b| > 20^\circ$. We used H I absorption data to constrain the physical nature of FIR/H I filaments and determine spin temperatures and volume densities of FIR/H I filaments. H I filaments exist as cold neutral medium (CNM) structures; outside the filaments no CNM absorption is detectable.

Conclusions. The CNM in the diffuse ISM is exclusively located in filaments with FIR counterparts. These filaments at high Galactic latitudes exist as cold density structures; velocity crowding effects are negligible.

Key words. clouds – ISM: structure – (ISM:) dust, extinction – turbulence – magnetic fields – magnetohydrodynamics (MHD)

1. Introduction

Take a teacup. At the bottom of this cup you can observe a caustic, the image of the Sun focused typically into two bright curves with a central peak. Caustics can also be generated by refraction, like a rainbow or the wiggling patterns at the bottom of a swimming pool. Simple structures of this kind can be explained by ray tracing.¹ Gravitational lensing and microlensing events are examples of more complex cases. The shapes of these caustics depend on the source distribution and the intervening matter (e.g., Blandford & Narayan 1992). Caustics are also found in topological structures of the cosmic web, such as voids, peaks, walls, and filaments (e.g., Bond et al. 1996). A general formalism for caustics that also applies to such complex structures has been given recently by Feldbrugge et al. (2018).

For the interpretation of caustics it is in general necessary to know some details of the physics of the imaging system as well as its geometry. This implies that some initial model assumptions are needed. Consent about model conditions is not always granted; different groups may advocate controversial models, and we are then faced with a diversity of possible interpretations. In this paper we discuss such a case, the interpretations

of observed caustics in the diffuse interstellar medium. Prominent filamentary structures, observable with *Planck* at 857 GHz or 353 GHz (Planck intermediate results XXXII. 2016; Planck intermediate results XXXV. 2016; Planck intermediate results XXXVIII 2016), are found to be well aligned with the ambient magnetic field in the diffuse interstellar medium (ISM). These small-scale structures caused by emission from dust in the far-infrared (FIR) are well aligned with small-scale H I structures and the discussion is about the nature of the observed intensity enhancements in H I channel maps.

One the one hand, these filamentary structures have been interpreted as caustics originating from real physical structures, coherent H I fibers with local density enhancements in position-velocity space. The ISM is understood as a multiphase medium with a diffuse warm neutral medium (WNM) in pressure equilibrium with the embedded cold neutral medium (CNM) (e.g., Wolfire et al. 2003). This CNM, observed with a characteristic narrow velocity distribution, is filamentary and associated with cold dust, stretched out along the magnetic field lines (e.g., Clark et al. 2014, Kalberla et al. 2016, Clark et al. 2019, or Peek & Clark 2019).

Counterarguments are based on Lazarian & Pogosyan (2000). The observed filaments accordingly indicate velocity caustics caused by turbulent velocity fluctuations. The observed intensity enhancements in channel maps with small velocity

¹ The first known drawing of these structures is by Leonardo da Vinci, available as Codex Arundel, folio 86, <https://www.bl.uk/catalogues/illuminatedmanuscripts/record.asp?MSID=6454>

widths originate in this approach from nonlinear density fields that are transformed by coherent turbulent velocities. The emission is generated in different volume elements, separated along the line of sight. Intensity enhancements are thus generated by velocity crowding. H I intensity enhancement may therefore not be interpreted as real coherent density structures, but reflect the properties of random turbulent fields. Such structures are referred to as velocity caustics

In this paper we discuss the two opposing positions. We focus on phenomena that lead to observable caustics in the diffuse interstellar medium. The scientific community needs to distinguish between the two different approaches that are described in almost identical terms, caustics and velocity caustics. In the first case we have generic caustics (*καυστική*), as introduced in the first paragraph. These caustics are deterministic. A particular source distribution generates a characteristic image, and a traceback is possible. In the second case of velocity caustics, intensity structures originate from turbulent velocity fluctuations. The statistical nature of this process does not allow conclusions about distinct source properties like temperature and volume density of the H I.

This paper is structured as follows. We first consider in Sect. 2 the morphology of generic caustics and the mathematical approaches that define such caustics. Next we discuss in Sect. 3 velocity caustics in context with the velocity channel analysis (VCA), proposed by Lazarian & Pogosyan (2000) and the derived velocity decomposition algorithm (VDA) by Yuen et al. (2021). In Sect. 4 we calculate the proposed VDA velocity and density contributions, and use the Hessian operator to determine VDA eigenvectors and orientation angles that are then compared with previous results from Kalberla et al. (2021, hereafter Paper I). The numerical results are discussed in Sect. 5; H I power spectra are discussed in Sect. 6. The physical conditions in caustics are considered in Sect. 7. We demonstrate that FIR/H I filaments are unambiguously related to the CNM and demonstrate the differences between velocity slicing and velocity tracing. After a summary in Sect. 8, we conclude that FIR/H I filaments can be traced as small-scale structures in position, associated with coherent structures in velocity with narrow linewidths. FIR/H I caustics are density structures in the position-velocity space.

2. Caustics: A morphological approach

Caustics are considered by mathematicians as part of the theory of local singularities of smooth morphisms; physicists are more interested in the stability of natural systems. In this context we start with a brief description of the mathematical background and methods that are useful for the determination and analysis of caustics.

2.1. Caustics as Morse complexes

Caustics are defined by their particular topology, and it is challenging to use a morphology-based data analysis to derive physical properties of observed intensity structures. The mathematical framework for a treatment of caustics is based on investigations by Thom (1975) and Arnold et al. (1985). Caustics are usually considered in the more general framework of catastrophe theory.² A recent rigorous treatment of the mathematical background can be found in Castrigiano & Hayes (2004). Caustics

² R. Thom received the Fields Medal in 1958 for his contributions to the topology of differentiable manifolds, and was later the founder of catastrophe theory.

in smooth differentiable maps are related to critical points, positions where the derivative of the investigated distribution function is zero. In 2D maps such positions identify minima, saddle points, and maxima. These are basins, passes, and peaks if we take mountain shapes as examples. These formations are usually structurally stable, and this is the property of generic critical points, also called Morse critical points, that can locally be approximated by quadratic functions. These points need to be nondegenerate, the determinant of the Hessian (the product of the eigenvalues) has to be nonzero. Thus, for our 2D application, structurally stable critical points are characterized locally by $x^2 + y^2$ (local minima), $x^2 - y^2$ or $y^2 - x^2$ (saddles), and $-x^2 - y^2$ (local maxima).

Caustics in more than two dimensions are far more complex. Structure analyses of the cosmic web need to take these general cases into account and have recently been discussed by Sousbie (2011), Sousbie et al. (2011), Feldbrugge et al. (2018), and Feldbrugge et al. (2019).³ Important for our 2D application is that generic caustics on the plane can only exist along A_3 caustics, as classified by Arnold, or cusps, which is the notation used by Thom (see Sect. 21.3, corollary 3 in Arnold et al. 1985). In general, the A_3 caustics characterize structures that are commonly labeled as filaments or fibers.

Filaments in the ISM have been described by Schisano et al. (2014) as elongated regions with a higher brightness contrast with respect to its surrounding. It is important that visual perceptions of this kind can be (and need to be) unambiguously verified as caustics. Such regions represent what is considered in the sense of a general morphological approach as descending manifolds, passes including connected peaks. Structures of this kind, A_3 caustics, can rigorously be extracted by using a Hessian-based filament identification scheme with negative eigenvalues. Alternatively to the Hessian matrix, different methods can be applied. The rolling Hough transform (RHT, Clark et al. 2014) and FILFINDER (Koch & Rosolowsky 2015) have been shown by Soler et al. (2020) to lead to equivalent results.

Formally, the set of all descending manifolds is usually referred to as the Morse complex (Sousbie 2011, definitions 2.4 and 2.5). Filamentary structures can be determined as surfaces of manifolds associated with critical points of order one (saddles) where the Hessian matrix has everywhere exactly one negative eigenvalue (described also as Morse index one). A peak is of order two.⁴ Peaks are isolated and are always connected to passes. Considering these peaks as parts of filaments (otherwise peaks would disrupt filaments) leads to the constraint that for filaments the Morse index must be at least one.

As discussed in Sect. 4, a number of publications since the year 2000 characterize filamentary structures in the ISM as velocity caustics in a rather unsharp and ambiguous way. This is in conflict with the original definition of caustics by Thom (1975) and Arnold et al. (1985), and for the sake of clarity in the following, in most cases we use the term filaments to describe A_3 caustics that are characterized by descending manifolds with Morse indices of one or two. Velocity caustics, caused by velocity crowding, have a filamentary appearance, but may not be considered to originate from homogeneous fibers, threads, or filaments.

³ A comprehensive introduction to catastrophe theory can be found at <https://jfeldbrugge.github.io/Catastrophe-Theory/>

⁴ FIR filaments with a threshold $\lambda_{\perp} < -1.5 \text{ Kdeg}^{-2}$, discussed in Paper I, have at high Galactic latitudes for 3% of all positions (6% all sky, respectively) a Morse index of two, and for 26% (39% all sky) an index of one.

2.2. The Hessian operator as applied to FIR and H I data

Morse complexes can best be identified with the Hessian matrix H , which is based on partial derivatives of the intensity distribution. This method was used for the first time by Polychroni et al. (2013) for the identification of filamentary structures in Orion A. Planck intermediate results. XXXII. (2016) used the Hessian matrix to study the relative orientation between the magnetic field and structures traced by interstellar dust. A recent application of this method to filamentary structures in the Galactic plane is presented in Soler et al. (2022).

In Paper I and Kalberla & Haud (2023, hereafter Paper II) high Galactic latitude structures in FIR and H I data were analyzed. Here we briefly summarize this approach. The Hessian matrix is defined as

$$H(x, y) \equiv \begin{pmatrix} H_{xx} & H_{xy} \\ H_{yx} & H_{yy} \end{pmatrix}. \quad (1)$$

Here x and y refer to the true angles in longitude and latitude. The second-order partial derivatives are $H_{xx} = \partial^2 I / \partial x^2$, $H_{xy} = \partial^2 I / \partial x \partial y$, $H_{yx} = \partial^2 I / \partial y \partial x$, and $H_{yy} = \partial^2 I / \partial y^2$.

The eigenvalues of H ,

$$\lambda_{\pm} = \frac{(H_{xx} + H_{yy}) \pm \sqrt{(H_{xx} - H_{yy})^2 + 4H_{xy}H_{yx}}}{2}, \quad (2)$$

describe the local curvature of the data (H I and FIR as described in Paper II). Eigenvalues $\lambda_{-} < 0$ K/deg⁻² with the associated eigenvectors are in direction of least curvature and indicate filamentary structures, passes, or ridges. We use negative thresholds for FIR and H I to identify only significant descending manifolds, hence caustics. The local orientation of filamentary structures relative to the Galactic plane (defined by the eigenvectors) is given by the angle

$$\theta = \frac{1}{2} \arctan \left[\frac{H_{xy} + H_{yx}}{H_{xx} - H_{yy}} \right], \quad (3)$$

in analogy to the relation

$$\theta_S = \frac{1}{2} \arctan \frac{U}{Q}, \quad (4)$$

from polarimetric observations that provide the Stokes parameters U and Q .

The Hessian analysis, including the determination of local orientation angles along the filaments, was applied in Paper I and Paper II to Planck FIR data at 857 GHz. Also considered were HI4PI H I observations (HI4PI Collaboration et al. 2016), combining data from the Galactic All Sky Survey (GASS; Kalberla & Haud 2015), measured with the Parkes radio telescope and the Effelsberg-Bonn H I Survey (EBHIS; Winkel et al. 2016) with data from the 100 m telescope.

The Hessian operator was applied to Planck 857 GHz FIR data with a threshold $\lambda_{-} < -1.5$ Kdeg⁻² to ensure the significance of the eigenvalues. This procedure defines an ensemble of isolated FIR filaments. In the next step this analysis was repeated for all H I channels, this time with an eigenvalue threshold $\lambda_{-} < -50$ Kdeg⁻². These limits take different sensitivities and intensity scaling in FIR and H I into account; we note that the applied thresholds are related to observed intensities due to the constant multiple rule for derivatives. Each of the FIR manifolds is found to be associated in H I with a distribution of filaments in velocity space (represented by channel maps) that approximately fit local shapes of the FIR structures. Orientation angles

θ were used to resolve the velocity ambiguities by searching for a velocity-space alignment of H I structures and orientation angles with the FIR emission.

Each individual FIR position within each of the descending manifolds was compared with each channel of the derived H I manifolds with the aim of finding the velocity with the best match for the local orientation angle θ . Best fit results, on average accurate to $\sigma_{\theta} = 4^{\circ}.1$, were found for narrow velocity channels with the original instrumental resolution at high Galactic latitudes, see Paper I. These morphologically derived velocities define the velocity field of the FIR filaments. Radial velocities along individual filaments were found to be well defined and coherent with an average random scatter of $\Delta v_{\text{LSR}} = 5.24$ km s⁻¹ along the filaments that was interpreted in Paper II as internal turbulent motions of the filaments.

In summary, the Hessian operator was used in Paper I to identify Morse complexes, filaments with common properties for FIR, and H I. Along these filaments FIR and H I share common orientation angles at well-defined coherent H I velocities. Known FIR distances allow volume densities to be determined from observed column densities. The Morse complexes can straightforwardly be interpreted as cold density filaments (see Paper II). Minkowski functionals were found useful to derive aspect ratios and filamentarity of the FIR/H I filaments.

3. Probing the velocity channel analysis

Velocity channel analysis (VCA, Lazarian & Pogosyan 2000) deals with emission spectra in individual velocity slices (channel maps) and derives dependences on the statistics of turbulent velocity and density fields by varying the slice thickness. Here we explain briefly the VCA preliminaries.

3.1. Velocity channel analysis and velocity caustics

H I and molecular line observations are usually organized in position-position-velocity (PPV) data cubes. Channel maps at constant velocities measure line intensities that depend on the physical conditions of the gas at a particular observed radial velocity. The derived parameters are affected by turbulent velocity fluctuations along the line of sight. Additional fluctuations in density are expected. The problem of disentangling velocity and density fluctuations was first addressed in Lazarian & Pogosyan (2000), and subsequently by Lazarian & Pogosyan (2004, 2006, 2008). These authors represent the PPV correlation function as a sum of two uncorrelated terms that depend for each velocity channel either on fluctuations of density or velocity. Accordingly, narrow velocity slices are supposed to be dominated by velocity perturbations and broad slices in the limit are dominated by column density effects. VCA aims in this way to disentangle velocity and density statistics. The claim after these investigations is that structures observed in narrow velocity intervals are caused predominantly by velocity caustics.

Generic caustics are associated with singularities of gradient maps. The most convenient way to search for caustics in 2D is the use of a Hessian-based filament identification scheme. Velocity caustics, generated by velocity crowding, were claimed to have been found in observations and magnetohydrodynamics (MHD) simulations by a number of authors (e.g., Esquivel et al. (2003), Chepurnov & Lazarian (2009), Padoan et al. (2009), Lazarian & Yuen (2018), and Ho & Lazarian (2023)). However, none of these publications provides a rigorous identification of structures as generic caustics or parts of Morse complexes in the

sense of Sect. 2.1 or as described by Thom (1975) and Arnold et al. (1985). In many cases numerical simulations ignore the thermal broadening of the lines that tends to wash out velocity fluctuations (see Clark et al. 2019, Sect. 3.1). Structures that are visible in simulated PPV maps in these cases are not representative for observed PPV maps.

3.2. Definition of the velocity decomposition algorithm

Following the theory by Lazarian & Pogosyan (2000), Yuen et al. (2021) developed a method for decomposing an observed PPV data cube into two separate cubes that are supposed to contain independently the turbulent velocity and density information. The decomposition is based on the postulate that in case of MHD turbulence the density and the velocity fluctuations are statistically uncorrelated. Using VDA notations this is formulated as $p = p_v + p_d$ with $\langle p_v p_d \rangle = 0$, for an ensemble average indicated by $\langle \dots \rangle$. The observed channel map⁵ p is decomposed in its velocity contribution p_v and density part p_d according to

$$\begin{aligned} p_v &= p - (\langle pI \rangle - \langle p \rangle \langle I \rangle) \frac{I - \langle I \rangle}{\sigma_I^2}, \\ p_d &= p - p_v \\ &= (\langle pI \rangle - \langle p \rangle \langle I \rangle) \frac{I - \langle I \rangle}{\sigma_I^2}, \end{aligned} \quad (5)$$

with $I = \int p(v) dv$ the total H I intensity (or column density) along the line of sight and $\sigma_I^2 = \langle (I - \langle I \rangle)^2 \rangle$. The necessary condition is that the velocity width Δv of the PPV channel map is small in comparison to the effective velocity width of the observed H I gas. To relate this condition to the analysis in Paper I we recall that $\Delta v = 1 \text{ km s}^{-1}$ was used there. Typical cold H I structures have a velocity width of 3 km s^{-1} , and thus H I is well resolved. VDA velocity fluctuations are noticeable only in narrow velocity intervals, but vanish if velocity slices get thicker; $p_v = 0$ for $\Delta v \rightarrow \infty$. Per the definition, VDA density fluctuations scale as $p_d \propto I$, in particular for low sonic Mach numbers $M_s \ll 1$ (Yuen et al. 2021, Sect. 3).

It is important to realize that Eq. (5) represents a decomposition of velocity and density fluctuations (positive or negative deviations from the mean), while the observed H I channel maps $p = p_v + p_d$ are density-weighted emission profiles. The differences between the two approaches are explained in Fig. 2 of Yuen et al. (2021). VDA densities p_d , although they are denoted as densities, are not to be confused with volume densities. This can be seen from Eq. (5), where p_v and p_d have the same units as p from observations. The brightness temperatures T_B in K averages over the width of the velocity channel in km s^{-1} . Volume densities demand a definition of the volume that is occupied by the H I (or modeling an object considered as a cloud). This definition is not part of the VCA or VDA concept. Volume densities in the presence of a dominating velocity crowding effect are in this context undefined.

According to Yuen et al. (2021), the term p_v in Eq. (5) represents the velocity contribution to velocity channels and is referred to as (or defined as) the velocity caustics contribution. Although they are called velocity caustics, p_v is not the velocity field; it can be seen only as a proxy for the part of the data that are (according to VCA/VDA) affected by the velocity field.

⁵ Observed data p are brightness temperatures T_B as weighted averages over the instrumental velocity window δv . For consistency with Yuen et al. (2021), we use p in place of T_B .

These velocity caustics p_v are not to be confused with caustics as defined by Thom (1975) or Arnold et al. (1985). To avoid any conflicts with caustics that are defined as manifolds in 2D, for p_v we use in the following the notation VDA velocity caustics. The observed data p , as well as the contributions p_v or p_d may contain manifolds that represent Morse complexes, but each p , p_v , or p_d velocity slice on its own represents no more than a smooth differentiable map that needs to be analyzed for the presence of supposed caustics before further conclusions can be drawn. Such an analysis is not part of VDA. VCA also does not attempt any morphological decomposition.

4. Hessian analysis of the VDA databases p_v and p_d

Following Eq. (5), we generate p_v and p_d for the observed p database used in Paper I. We repeat the complete Hessian analysis described in Sect. 2 of Paper I independently for VDA derived velocity p_v and density p_d structures without modifying any of the program parameters. In the following we discuss the properties derived from Hessian eigenvalues and eigenvectors independently.

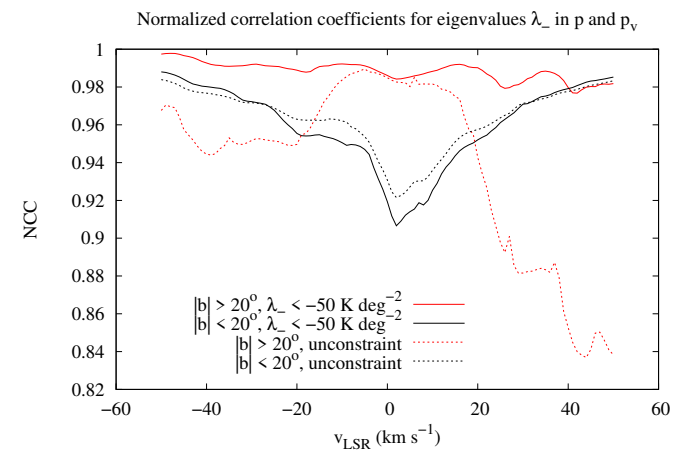


Fig. 1. Normalized correlation coefficients for eigenvalues in observed intensity p and VDA velocity caustics p_v , according to Eq. (5) at high and low Galactic latitudes. Data constrained by $\lambda_- < -50 \text{ K deg}^{-2}$ (used in Paper I to compare H I with FIR filaments) and unconstrained eigenvalues are distinguished.

4.1. Correlations of λ_- eigenvalues in p and p_v

Inspecting derived eigenvalues for λ_- in p and p_v visually, we find a close agreement between the two distributions. The correlation between the A and B distributions can, according to Yuen et al. (2021), be best verified by using the normalized covariance coefficient

$$NCC(A, B) = \frac{\langle (A - \langle A \rangle)(B - \langle B \rangle) \rangle}{\sigma_A \sigma_B} \quad (6)$$

to characterize correlations between the two 2D maps A and B ; here we use the same notations as Yuen et al. (2021). This measure, also known as Pearson product-moment correlation coefficient, is scale-invariant and results in $NCC(A, B) \in [-1, 1]$. The case $NCC(A, B) = 0$ implies that the two maps are statistically uncorrelated. A perfect correlation requires that $NCC(A, B) = \pm 1$; the sign reflects the slope of the linear regression that can be fitted in this case.

The correlation coefficients $NCC(\lambda_-(p), \lambda_-(p_v))$ for the eigenvalue distributions at all velocity channels $-50 < v_{\text{LSR}} < 50 \text{ km s}^{-1}$ are shown in Fig. 1. The best correlations with $NCC(\lambda_-(p), \lambda_-(p_v)) \gtrsim 0.98$ are found at latitudes $|b| > 20^\circ$ in the case of filamentary structures constrained in H I by $\lambda_- < -50 \text{ K deg}^{-2}$. This is the same condition as used in Paper I to ensure that H I filaments are unaffected by observational uncertainties. Unconstrained $\lambda_-(p)$ and $\lambda_-(p_v)$ eigenvalue distributions at high latitudes show only a perfect correlation for $|v_{\text{LSR}}| \lesssim 8 \text{ km s}^{-1}$; this is the velocity range with dominant CNM filaments (see Fig. 11 in Paper I). The $\lambda_-(p)$ and $\lambda_-(p_v)$ eigenvalue distributions at low Galactic latitudes suffer from confusion (Paper II, Sect. 3.1) and the correlation $NCC(\lambda_-(p), \lambda_-(p_v))$ degrades significantly, whether they are constrained or not.

After discussing the general correlation analysis on Galactic scales we display on top of Fig. 2 an example for the eigenvalue distribution $\lambda_-(p_v)$ together with deviations $\lambda_-(p_v) - \lambda_-(p)$. Minor deviations are visible, they reflect the result that the eigenvalues λ_- for p and p_v at high Galactic latitudes are highly similar. At the bottom of Fig. 2 we display for comparison the velocity field of the FIR filaments derived from p_v , together with deviations from the velocity field published in Paper I.

The Hessian analysis of the VDA velocity term p_v , using exactly the same procedures as in Paper I, recovers in 97% of all case positions in the Morse complexes that are identical with the positions of the filamentary structures found in Paper I. Less than half (43%) of the previously derived filament positions have identical VDA filament velocities but for 53% of them the differences are below 1 km/s. Allowing uncertainties of $\Delta v \lesssim 6 \text{ km s}^{-1}$ for the filament velocities (see Sect. 2.6 of Paper I), we obtain compatible velocities for 68% of all filament positions. A close inspection of the lower part of Fig. 2 reveals that positions with significant differences in the derived velocities are located predominantly on the filament outskirts. In comparison to the filament centers, these positions have a lower signal-to-noise ratio (S/N). We also note an increase in the velocity uncertainties toward the Galactic plane, explainable with increasing confusion due to the increasing complexity of the H I emission.

4.2. Orientation angle alignments between θ_{p_v} , θ_p , and θ_{FIR}

In the previous subsection we considered agreements in eigenvalues λ_- . In the following we take the eigenvectors into account. These determine the local orientation of filamentary structures and are conveniently parameterized by the angle θ according to Eq. (3). We complete the comparison between filamentary structures in p_v and p with a summary of orientation angle alignments in Table 1 and Fig. 3. To allow an easy comparison, we replicate the previously derived best fit entries from Fig. 3 and Table 1 of Paper I.

For a detailed definition of the different alignment measures in Table 1 we refer to Paper I. Here we provide only a brief description. To measure the angular alignments between two data sets we calculate first the angular difference between the orientation angles Θ_1 and Θ_2 at each position:

$$\delta\theta = \frac{1}{2} \arctan \left[\frac{\sin(2\theta_1)\cos(2\theta_2) - \cos(2\theta_1)\sin(2\theta_2)}{\cos(2\theta_1)\cos(2\theta_2) + \sin(2\theta_1)\sin(2\theta_2)} \right]. \quad (7)$$

The width of the resulting $\delta\theta$ distribution, shown in Fig. 3, can be measured by fitting either a Gaussian or a Voigt function; the Voigt function approximates noisy data best. Table 1 lists the fitted $\delta\theta$ dispersions σ_{Gauss} and σ_{Voigt} . The mean degree of alignment, $\xi = \langle \cos\phi \rangle$, can be defined for $\phi = 2\delta\theta$ (Clark & Hensley

2019). A different metric, the projected Rayleigh statistic (PRS), was calculated according to Jow et al. (2018),

$$\text{PRS} = \sqrt{\frac{2}{N}} \sum_i \cos \phi_i, \quad (8)$$

and the uncertainty of this measure is estimated as

$$\sigma_{\text{PRS}}^2 = \frac{2 \sum_i \cos^2 \phi_i - (\text{PRS})^2}{N}. \quad (9)$$

Equation (8) approximates the more general Eq. (4) of Soler et al. (2022) in the case of constant statistical weights. This is justified to a high degree for the all-sky surveys in FIR and H I that we are using here.

The distributions of angular alignment deviations according to Eq. (5) of Paper I between orientation angles of FIR filaments and H I structures are very similar if we use the VDA p_v in place of observed H I brightness temperatures p . The best fit result for the velocity width of the slices used, presented in Sect. 2 of Paper I, remains valid and is obtained when using H I channel maps with a velocity width of $\Delta v = 1 \text{ km s}^{-1}$. Filamentary structures in the VDA velocity caustics p_v have a $\sim 30\%$ broader $\delta\theta$ distribution compared to the best fit distribution obtained from observed H I channel maps p (see the widths of the distributions in Fig. 3 and the dispersions σ_{Gauss} and σ_{Voigt} in Table 1). The angular alignment deviations for the VDA density distribution p_d (Fig. 3 bottom) are unacceptably large, and the filling factors $f = 0.04$ in Table 1 are extremely low. The sky contains a negligible amount of filaments from the VDA p_d distribution. The VDA densities p_d are derived from scaled H I column densities according to Eq. (5), and we found already in Sect. 2 of Paper I that integrating the H I distribution does not lead to an improvement in the angular alignment measures.

5. Evaluation: Caustics in p_v contra p

After an introduction to morphological concepts that define caustics according to Thom (1975) or Arnold et al. (1985), we discussed methods to derive caustics. We also introduced VDA, derived the databases according to the VDA technique and calculated caustics of the VDA databases. These results were compared with caustics from H I data in conventional PPV databases. In both cases we correlated FIR caustics with H I caustics. Based on these preliminaries, in the following we discuss the mathematical issues and controversial interpretations with respect to the physical nature of the FIR/H I filaments.

5.1. Velocity caustics p_v are not caustics

The paper by Yuen et al. (2021) specifies in detail how the concept of VCA velocity caustics can be applied numerically to observations (see Sect. 3.2). With this definition of VDA velocity caustics p_v for the first time it becomes possible to elaborate the VCA concept of velocity caustics in detail. Section 4 shows that VDA velocity caustics p_v according to Eq. (5), despite their name, are not caustics as defined by Thom (1975) or Arnold et al. (1985). To be clear, structures have been defined as velocity caustics without any concern about the verification of these structures as caustics (descending manifolds) in the usual topological meaning.

In a way similar to the observed distribution p , the VDA descendants p_v and p_d may contain morphological structures that

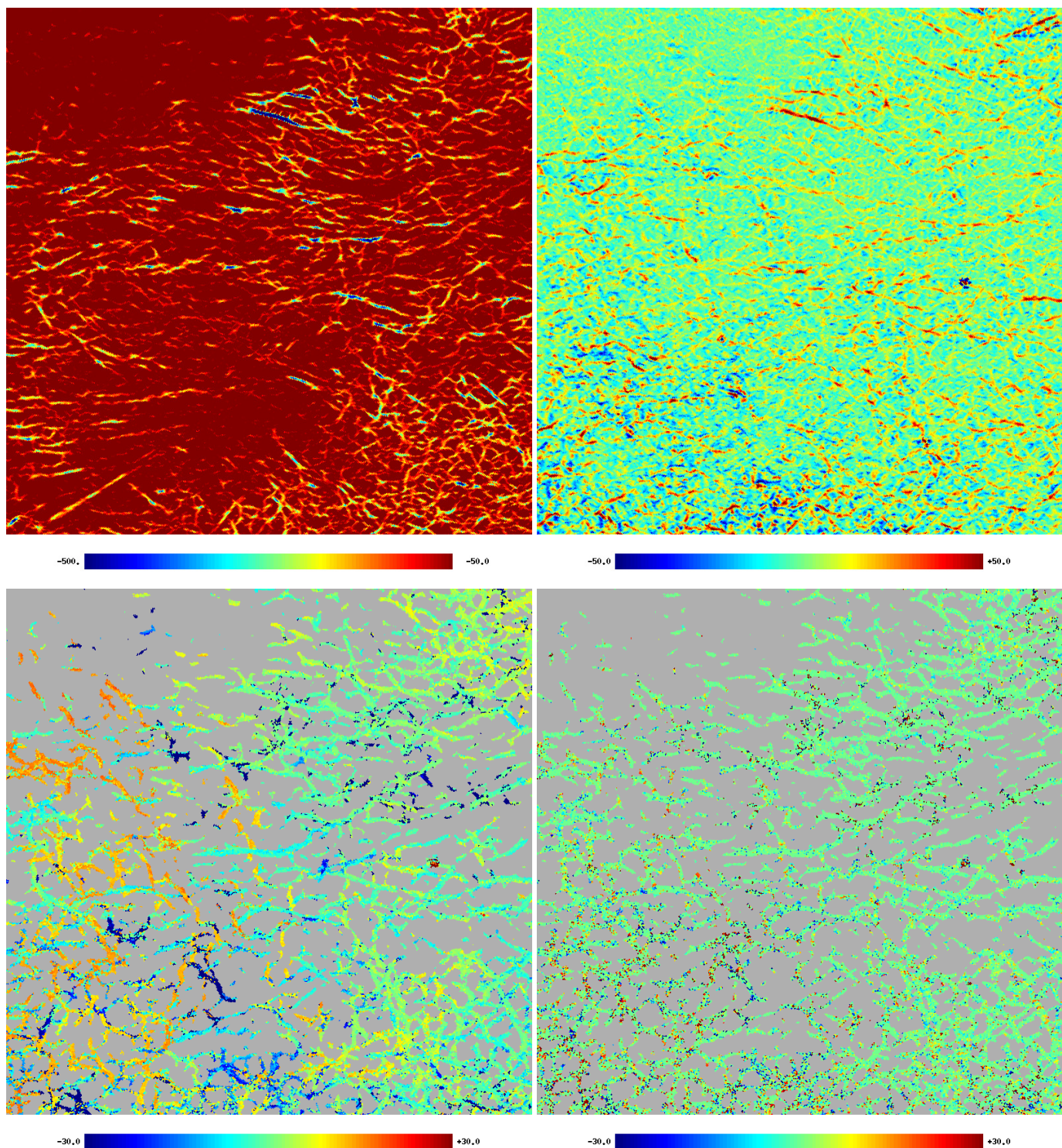


Fig. 2. Display of example data in gnomonic projection. The field center is at $l = 160^\circ$, $b = 30^\circ$, the field size $27:7$. Top left: eigenvalues $\lambda_{-}(p_v)$ of VDA velocity caustics p_v at $v_{\text{LSR}} = 0 \text{ km s}^{-1}$. Top right: deviations $\lambda_{-}(p_v) - \lambda_{-}(p)$ between eigenvalues from VDA velocity caustics p_v and observed intensities p . Bottom left: velocities $v_{\text{LSR}}(p_v)$ of filamentary FIR structures in case of H I filaments derived for VDA velocity caustics p_v . Bottom right: deviations $v_{\text{LSR}}(p_v) - v_{\text{LSR}}(p)$ from the velocity field $v_{\text{LSR}}(p)$ shown in Fig. 6 of Paper I.

can be identified as caustics. These particular subsets (or manifolds that can be considered A_3 caustics) need to be determined according to the restrictions explained in Sect. 2.1. For this purpose we applied the Hessian operator, and we show in Sect. 4 that p and p_v contain essentially identical filamentary structures.

However, when matching filamentary H I structures to FIR caustics, the alignment of VDA p_v structures is less accurate by 30%.

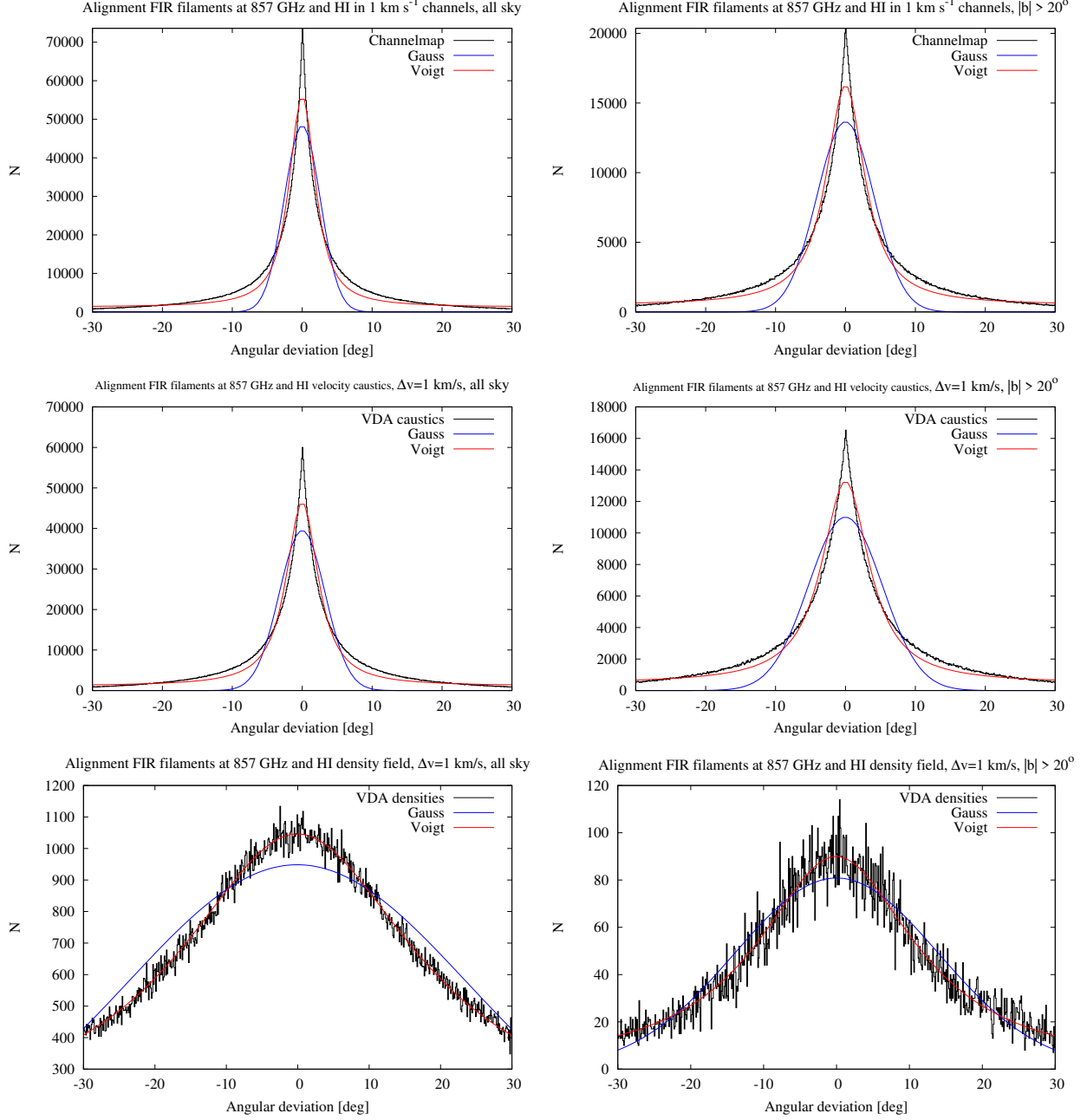


Fig. 3. Histograms of angular alignment deviations according to Eq. (5) in Paper I for filamentary structures. Top left: *Planck* 857 GHz compared with best fit single-channel HI filaments, all sky. Top right: *Planck* 857 GHz compared with best fit single-channel HI filaments, $|b| > 20^\circ$. These two plots were replicated from Fig. 3 in Paper I. Center left: *Planck* 857 GHz compared with best fit filaments from the VDA velocity field p_v , all sky. Center right: *Planck* 857 GHz compared with best fit filaments from p_v with $|b| > 20^\circ$. Bottom left: *Planck* 857 GHz compared with best fit filaments from the VDA density distribution p_d , all sky. Bottom right: *Planck* 857 GHz compared with best fit filaments from the VDA density distribution p_d , $|b| > 20^\circ$.

Table 1. Filamentary alignment measures, for comparison with Table 1 in Paper I

Data 1	Data 2	latitude range	f	$\delta\theta$	ξ	PRS	σ_{PRS}	Fig.	
<i>Planck</i> 857 GHz	HI4PI								
18' FWHM	HI in 1 km s^{-1} channels	all	.37	2:6	1:9	0.94	2873.67	.17	3 top left
18' FWHM	VDA velocity field p_v	all	.37	3:3	2:5	0.94	2856.50	.18	3 middle left
18' FWHM	VDA density field p_d	all	.04	23:8	20:2	0.76	786.92	.38	3 bottom left
18' FWHM	HI in 1 km s^{-1} channels	$ b > 20^\circ$.24	4:1	3:1	0.92	1817.64	.23	3 top right
18' FWHM	VDA velocity field p_v	$ b > 20^\circ$.23	5:3	3:9	0.91	1789.17	.24	3 middle right
18' FWHM	VDA density field p_d	$ b > 20^\circ$.04	14:0	13:1	0.84	207.28	.31	3 bottom right

5.2. Caustics in p and p_v as local diffeomorphisms

Caustics in 2D maps are descending manifolds, associated in case of the observed FIR/H I filamentary structures predominantly with local structures of index one (Sect. 2.1). According to the Morse lemma, these regions can locally be approximated by quadratic functions. These local coordinate transformations describe local diffeomorphisms (Castrigiano & Hayes 2004). Generic critical points are structurally stable, allowing a smooth transition and approximation by quadratic functions. Essential for such an approximation in 2D is that the Hessian matrix has to be nondegenerate. The index of a nondegenerate critical point fully classifies the critical point up to coordinate transformations. The Hessian, Eq. (1), is determined from second derivatives and describes the local curvature. Inspecting Eq. (5), it is easy to see that p_v and p_d are derived from p by smooth linear transformations, essentially by subtracting mean intensities and rescaling. The terms $\langle p|I \rangle$ and $\langle p \rangle \langle I \rangle$ in Eq. (5) are constants, applied to the scaling factor $(I - \langle I \rangle) / \sigma_I^2$. Linear transformations as in Eq. (5) do not affect the Morse index significantly. Thus, common Morse complexes derived for p and p_v represent local diffeomorphisms, explaining the high correlation coefficients $NCC(\lambda_-(p), \lambda_-(p_v)) \gtrsim 0.98$ (see Fig. 1) at high Galactic latitudes.

The concept of local diffeomorphisms simply implies that the transition from p to p_v is defined by a smooth transformation under the condition that the two maps remain differentiable. In other words, two singularities are considered equivalent if and only if there exists a local transformation that maps them into each other. This applies to 97% of the caustics in p that replicate as local diffeomorphisms in p_v .

Understanding Morse complexes, derived from p and p_v databases, as local diffeomorphisms, the assertion that the VDA could derive a completely new set of unexplored velocity caustics data from every spectroscopic data set (Yuen et al. 2021, Sect. 11, item 9) needs to be questioned. The results from Sect. 4, summarized in Table 1 and Fig. 3, indicate that the best alignment between FIR and H I filaments exists for the original unmodified brightness temperatures p . The correlation between filaments in FIR and VDA velocity caustics p_v is weaker, indicating that the VDA algorithm does not quite match the physics of the filamentary ISM.

6. VDA power distributions: P_v and P_d contra P

A fundamental VCA postulate is that turbulent density and velocity fields are statistically uncorrelated for the case of MHD turbulence (Lazarian & Pogosyan 2000, Sect. 6.3.1, Appendix B). For purely isothermal turbulent media global density-velocity correlations are unexpected. Federrath & Banerjee (2015) show however that for non-isothermal multiphase media the Mach number correlates with the gas density (their Fig. 7). Understanding the Mach number as a proxy for turbulent velocities, one expects, depending on the equation of state, that the statistics of velocity and density fluctuations are not independent. The VDA algorithm, Eq. (5), depends by construction on the mathematical definition $\langle p_v p_d \rangle = 0$ regardless of any actual physics. It is highly misleading to present this relation as an observational fact, as is done by Hu et al. (2023) in their Appendix A.

Assuming independence of density and velocity, VDA aims to separate the contributions arising from density and velocity fluctuations with the corresponding power spectra $P = P_v + P_d$. For an evaluation of systematic differences in the power spec-

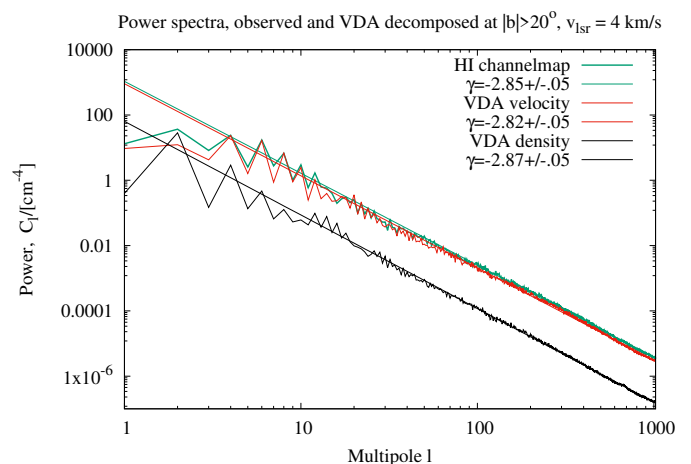


Fig. 4. Turbulent power spectra for the observed H I emission p at high Galactic latitudes at a velocity of $v_{\text{LSR}} = 4 \text{ km s}^{-1}$ compared with power spectra derived from VDA velocity and density contributions p_v and p_d .

tra we calculate the averages of P_v and P_d at high Galactic latitudes. We also relate these contributions to the power P from the raw observations. According to Lazarian & Pogosyan (2000) such power spectra should be steep with power law indices $\gamma < -3$. Power law indices derived from channel maps are velocity dependent. To match VCA expectations, we therefore use the steepest power spectra at a velocity of $v_{\text{LSR}} = 4 \text{ km s}^{-1}$ derived from HI4PI data (see Kalberla & Haud 2019, Fig. 9). For the VDA velocity power spectrum P_v we obtain a power law index $\gamma_v = -2.82 \pm 0.05$, almost identical with $\gamma_{\text{obs}} = -2.85 \pm 0.05$ from the observed H I channel map at the same velocity (see Fig. 4). The spectral index $\gamma_d = -2.87 \pm 0.05$ for the VDA density is by definition velocity independent and identical to the power law index of the total column density distribution. In summary, Fig. 4 implies that the spectral indices for P , P_v , and P_d are, within the uncertainties, identical. All power spectra are straight and do not show any bending in contrast to different possible model contributions in P_v and P_d (see the case studies in Figs. 6 and 7 of Lazarian & Pogosyan 2000). The predicted systematical spectral index changes between P_v , P_d , and P (their Table 1) are not observed.

Velocity decomposition algorithm density fluctuations are marginal and provide only 4% of the observed power. This low level is within the uncertainties consistent with the previous finding (Sect. 4) that Morse complexes of p_v recover 97% of the positions in Morse complexes of p . Fig. 4 shows that the power distributions for p and p_v are almost identical. The derived spectral index $\gamma \sim -2.85$ is representative of individual probes of the ISM at high Galactic latitudes (see Fig. 9 in the review by McClure-Griffiths et al. 2023). An average index of $\gamma \sim -2.85 \pm 0.02$ has also been derived by Mittal et al. (2023) after correcting the H I distribution for differences in H I path lengths along the line of sight (see their Fig. 8). Under the VCA constraint that the velocity with the steepest power spectrum should be selected, the decomposition of the observed brightness temperature distribution in VDA velocity caustics p_v and densities p_d does not alter the observed spectral index from P . This result is consistent with the investigations in Sect. 4. Statistical similarities in P and P_v reflect general morphological similarities in p and p_v .

7. The physics of FIR/H I Morse complexes

The data that are analyzed in [Paper I](#) suggest that filamentary FIR and H I structures, observable at high Galactic latitudes, were shaped by a Galactic small-scale dynamo. This conclusion is based on the filament curvature distribution along the filaments ([Paper I](#), Sect. 4). Furthermore, individual filament-like structures share common morphological properties. Filamentary structures are not individuals; they share a network of filaments. The resulting distribution of aspect ratios \mathcal{A} and filamentarities is well defined and continuous without clear upper limits in \mathcal{A} ([Paper II](#)). The question arises whether common morphological properties arise from common physical conditions. The FIR filament emission is broadband, but in H I the structures are best reproduced in narrow velocity intervals.

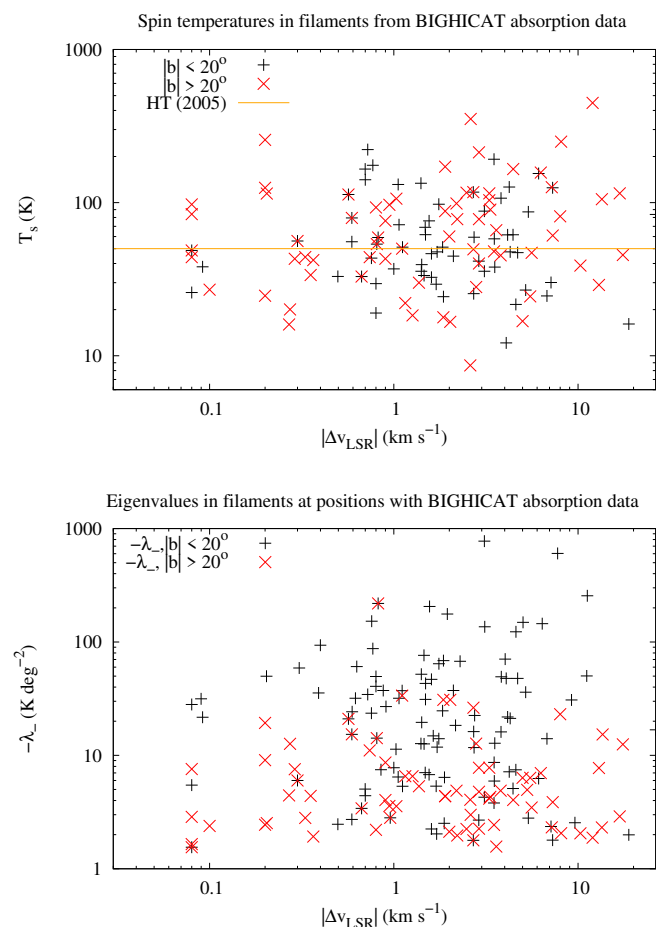


Fig. 5. Parameters derived from BIGHICAT data for absorption components with closest match in filament velocities with deviations of $|\Delta v_{\text{LSR}}|$ km s $^{-1}$ between absorption and emission components. Top: Spin temperatures T_s in filaments. The horizontal line indicates the characteristic spin temperature $T_s = 50$ K, derived by [Heiles & Troland \(2005\)](#). Bottom: Eigenvalues $-\lambda_-$ for the same sample.

7.1. Spin temperatures and volume densities in H I filaments

In [Paper I](#) it was shown that filaments in H I have low Doppler temperatures. Such temperatures are derived from emission data, and hence the observed line widths are broadened by turbulent motions and the derived Doppler temperatures are only upper limits to the spin temperatures of the H I. With the advent of sen-

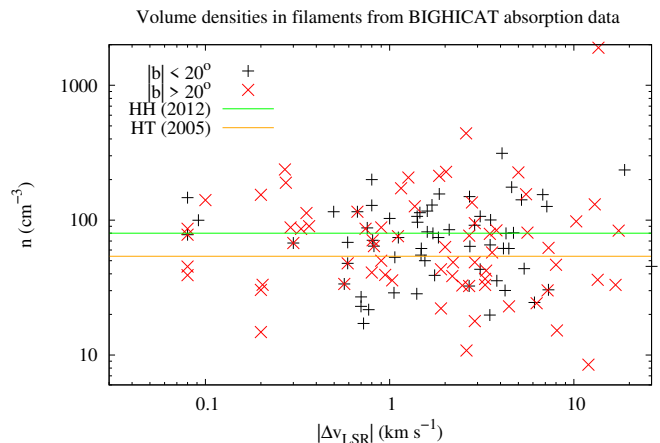


Fig. 6. Volume densities n in filaments from BIGHICAT data for absorption components with the closest match in filament velocities with deviations of $|\Delta v_{\text{LSR}}|$ km s $^{-1}$ between absorption and emission components. The horizontal lines indicate the characteristic volume densities of $n = 80$ cm $^{-3}$ derived by [Heiles & Haverkorn \(2012\)](#) and $n = 54$ cm $^{-3}$ by [Heiles & Troland \(2005\)](#).

sitive absorption surveys it has become feasible to probe FIR/H I filaments for spin temperatures. [McClure-Griffiths et al. \(2023\)](#) collected BIGHICAT, a catalog with 372 unique lines of sight, providing spin temperatures, optical depth, and other properties. We use BIGHICAT to probe spin temperatures within filaments and outside. Figure 3 of [McClure-Griffiths et al. \(2023\)](#) shows the spatial distribution of the absorption components.

BIGHICAT contains 66 positions without detectable absorption; 63 of these positions (95%) are located outside FIR/H I filaments. These 63 positions probe only WNM, which is known to be ubiquitous. The WNM is known to contain no significant small-scale structures, and also has a very low optical depth. From the remaining sources 122 positions need to be disregarded because the associated FIR eigenvalues exceed the threshold $\lambda_- > -1.5$ K/deg $^{-2}$. A total of 37 positions from BIGHICAT close to the Galactic equator are without available spin temperatures, but in 23 of these cases we were able to replace these data by using Gaussian components from the HI4PI survey. This way 174 positions from the absorption survey could be used to determine absorption components at velocities with the closest agreement to observed local filament velocities. These components represent the local physical conditions along the line of sight that are representative for significant FIR/H I filaments. Figure 5 shows the resulting spin temperatures as a function of velocity deviation $|\Delta v_{\text{LSR}}|$. These velocity deviations represent differences in velocity between the pencil beam pointing to the background source and the closest HI4PI survey position within a filament. Thus, the detectable velocity differences $|\Delta v_{\text{LSR}}|$ represent turbulent velocity fluctuations on scales below 3'.4.

The spin temperatures in Fig. 5 occupy a range $10 \lesssim T_s \lesssim 500$ K, values that are, according to [Wolfire et al. \(2003\)](#), characteristic for the temperature of the CNM. [Heiles & Troland \(2005\)](#) derived a typical CNM temperature of 50 K. The lower display of Fig. 5 shows that these low temperatures are associated with significant FIR eigenvalues in $-\lambda_-$. There is a trend for lower spin temperatures at positions with lower eigenvalues λ_- , but the available data are currently insufficient to establish a significant correlation ($r = 0.33$). [McClure-Griffiths et al. \(2023\)](#) expect that as soon as the Square Kilometer Array is in full operation, the number of entries in BIGHICAT will increase by several orders

of magnitude. Thus, the significance of this correlation can be tested within a few years.

The typical conditions for the CNM in the local multiphase ISM in thermal equilibrium with the WNM can, according to [Jenkins & Tripp \(2011\)](#), be determined from an equilibrium pressure of $\log(p/k) = 3.58$. This results in a typical CNM excitation temperature of 80 K, consistent with [Fig. 5](#). The cooling time for the ISM is in this case estimated by [Jenkins & Tripp \(2011\)](#) to $3 \cdot 10^4$ yr. This timescale is short in comparison to the timescale for the growth of the small-scale magnetic energy, characterized by the viscous eddy turnover time in the order of 10^5 yr ([Schekochihin et al. 2004](#)). The spin temperature depends on excitation processes for the 21 cm line and can for the CNM usually be equated to the excitation temperature ([McClure-Griffiths et al. 2023](#), Sect. 2). Volume densities, derived from absorption observations, are based on the assumption of a local thermal equilibrium. CNM filaments had sufficient time to reach thermal equilibrium, and therefore BIGHICAT data can be used to derive realistic volume densities. The results are shown in [Fig. 6](#); the volume densities are again typical for the CNM, and agree well with the estimates $n = 54 \text{ cm}^{-3}$ and $n = 80 \text{ cm}^{-3}$ by [Heiles & Troland \(2005\)](#) or [Heiles & Haverkorn \(2012\)](#), respectively. The available sample of absorption features support the interpretation of filaments as cold dense CNM structures. Outside the filaments no absorption and no CNM is detectable.

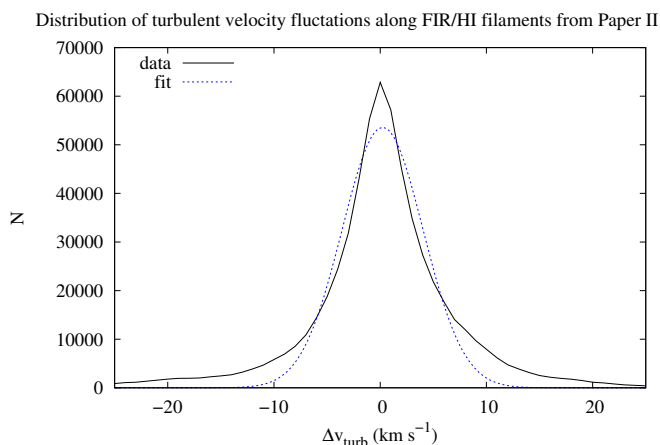


Fig. 7. Distribution of turbulent velocity fluctuations Δv_{turb} along filaments for the sample used in [Paper II](#). The Gaussian fit has a velocity dispersion of $\sigma = 3.8 \pm 0.1 \text{ km s}^{-1}$.

7.2. Turbulent velocity fluctuations

As detailed in [Sect. 2.2](#), H I filaments were matched to FIR filaments using both Hessian eigenvalues and orientation angles (deduced from eigenvectors). In [Paper II](#) the resulting set of Morse complexes was decomposed in 6568 individual FIR/H I filaments. For each of these filaments an average radial velocity $\langle v_{\text{fil}} \rangle$ was determined. Along each of the H I filaments fluctuating radial velocities were observed. We consider these fluctuations as an imprint of the turbulent velocity field $\Delta v_{\text{turb}}(l, b) = (v_{\text{fil}}(l, b) - \langle v_{\text{fil}} \rangle)$ by subtracting for each filament position the average radial velocity $\langle v_{\text{fil}} \rangle$ from the local filament velocity $v_{\text{fil}}(l, b)$. [Figure 7](#) shows the distribution of Δv_{turb} . The observed turbulent velocity dispersion is $\sigma = 3.8 \pm 0.1 \text{ km s}^{-1}$. This is low in comparison to the expected dispersion $\sigma \sim 10 \text{ km s}^{-1}$ in the turbulent ISM ([Burkert 2006](#)). The observed Δv_{turb} distribu-

tion is not uniform, however; the median dispersion is $\Delta v = 5.24 \text{ km s}^{-1}$. [Figure 12](#) in [Paper II](#) shows that filaments with low aspect ratios can have a low velocity dispersion but prominent filaments, with high aspect ratios and covering large surface areas, have enhanced velocity dispersions. These approach the limit $\sigma \sim 10 \text{ km s}^{-1}$. We also note the extended wings in [Fig. 7](#), indicating some local misidentifications in the FIR/H I filaments causing uncertainties in the determination of filament velocities.

Extended cold H I filaments with a typical linewidth of 3 km s^{-1} (e.g., [Paper II](#), Sect. 3.1) that are exposed to turbulent velocity fluctuations of 3.8 to 10 km s^{-1} are affected necessarily by shifts in observed radial velocities. Filaments that are observed in channel maps with a velocity width of 1 km s^{-1} appear disrupted, and filaments appear to have low aspect ratios. Within PPV channel maps, filament elements that are affected by turbulent velocity fluctuations shift frequently from one velocity channel to another. This leads to an apparent fragmentation and lowers aspect ratios if only channel maps are considered.

Tracing the FIR orientation angle in H I recovers the PPV_{fil} filament geometry in the plane of the sky. Both FIR and H I filaments share common orientation angles. FIR filaments are observed in broadband and the FIR orientation angles are not affected by velocity fluctuations. Tracing FIR orientation angles in H I by fitting (velocity dependent) orientation angles tells us the velocity of the FIR filaments ([Clark & Hensley 2019](#) and [Paper II](#), Sect. 3.3). Thus, the 3D PPV geometry is modified for each individual filament to the 2D case PPV_{fil} , where V_{fil} stands for the position-dependent filament velocity across the PPV cube. The transformation from PPV to PPV_{fil} represents for each individual filament a smooth transformation (or deformation) of the velocity space. Magnetic fields associated with the filaments suffer from foldings that cause magnetic tension forces with back reactions on the turbulent flow ([Schekochihin et al. 2004](#)). In such a scenario, density structures need to be understood as structures in l, b, v_{LSR} , and hence with PPV_{fil} morphology. Each filament occupies an individual PPV_{fil} space. The width of the V_{fil} slice depends on the observed CNM line width, and is typically 3 km s^{-1} . The Morse complexes that we analyzed need to be understood as manifolds in PPV_{fil} . Since the filaments are disjunct in position, an all-sky PPV_{fil} distribution can be derived.

7.3. VCA velocity mapping in slices

VCA and VDA are theories that are strictly designed for a PPV geometry, decomposing the emission in velocity slices of variable thickness. The claim is that VCA allows a separation of velocity and density fields that affect the PPV data cube, depending on the thickness of the velocity slice. This theory does not allow a local transition of distinct homogeneous filament structures from PPV to PPV_{fil} . The expected role of (hydrodynamic) turbulence is to induce velocity crowding. Filamentary structures are understood as velocity caustics, caused by velocity crowding along the line of sight. Spatially distributed H I along the line of sight is affected by turbulent velocities and mimics density structures in this way. Thus, turbulence moves separate H I components into the same velocity coordinate in PPV space, leading to a merging of these components into a single structure (e.g., [Hu et al. 2023](#), [Fig. 1](#)). VCA velocity mapping does not allow us to interpret filamentary structures as real physical objects.

The spectrum of eddies that correspond to most of the turbulent energy at large scales corresponds to the spectrum of thin channel map intensity fluctuations having most of the energy at small scales ([Kandel et al. 2016](#)). [Lazarian & Yuen \(2018\)](#) con-

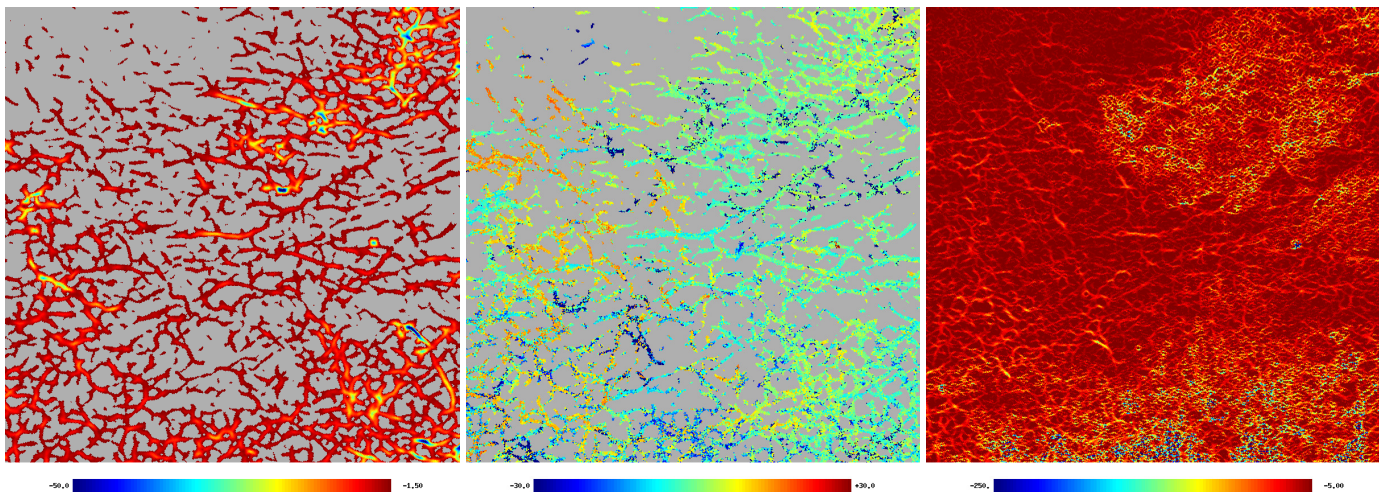


Fig. 8. Examples for structures derived with different methods, coordinates are identical with Fig. 2. Left: filaments derived for 857 GHz FIR data in Paper II, shown are eigenvalues $-50 < \lambda_- < -1.5 \text{ K/deg}^{-2}$. Center: PPV_{fil} with color coding in velocity, representing the corresponding velocity field in the range $-30 < v_{\text{LSR}} < 30 \text{ km s}^{-1}$. Right: caustics in H I column density maps from Paper II, integrated from $-50 < v_{\text{LSR}} < 50 \text{ km s}^{-1}$ with eigenvalues $-250 < \lambda_- < -5 \text{ K/deg}^{-2}$.

clude that on scales larger than 3 pc, the intensity of fluctuations in the channel maps is produced to a significant degree by velocity caustics rather than real physical entities (i.e., filaments). This 3 pc scale, derived by Lazarian & Yuen (2018) for a turbulent energy cascade with a steep power spectrum, can be compared with the filament widths of 0.63 pc derived in Paper II for an average filament distance of 250 pc. Velocity mapping is affected by projection effects, but must be spatially coherent in direction perpendicular to the filament. HI4PI data constrain this coherence to 0.63 pc, otherwise the filamentary structures would be smoothed out.

The VCA velocity mapping of distributed H I components along the line of sight to the observed PPV space has consequences for models of the internal structure of FIR filaments. Broadband observations of thermal dust emission are sensitive to the density field, but not to velocity. For FIR/H I filaments the velocity crowding effect implies that several distinct turbulence induced dust components must exist along the line of sight. This is in clear contrast to FIR/H I filaments as coherent structures in PPV_{fil} . Planck intermediate results XLIV. (2016) consider FIR filaments in the diffuse ISM at high Galactic latitudes as density structures; in addition, Planck intermediate results. XXXII. (2016) consider them as ridges that are at high Galactic latitudes usually aligned with the magnetic field measured on the structures.

7.4. FIR filaments and the H I haystack

VCA is based on the analysis of velocity slices with variable thickness, spanning from thin to very broad velocity slices with structures in column density, and claims to reconstruct the underlying velocity and density characteristics. This approach fails, and as a demonstration we want to compare a basic subset of Morse complexes with very thick and thin velocity slices with FIR caustics. Figure 8 first compares FIR filaments with our derived PPV_{fil} results and eigenvalues for H I column densities integrated over the range $-50 < v_{\text{LSR}} < 50 \text{ km s}^{-1}$. Instead, Fig. 9 covers H I eigenvalues λ_- for channel maps with a 1 km s^{-1} channel width at velocities $-4 < v_{\text{LSR}} < 4 \text{ km s}^{-1}$. Fluctuations of the eigenvalue strengths along the filaments are frequent.

7.5. Filament tracing contra velocity slicing

The FIR filaments in the left panel of Fig. 8 are clearly well represented by a rather continuous PPV_{fil} distribution with a well-defined homogeneous velocity structure, including some turbulent velocity fluctuations. This is the result from Paper I, matching FIR and H I structures with both eigenvalues and orientation angles (from eigenvectors). The best fit result was obtained by using local velocity slices with a thickness of 1 km s^{-1} . Increasing the velocity slice thickness leads to a degradation of the results. Comparing FIR filaments (left in Fig. 8) with filaments in column density eigenvalues (right), we find a very complex distribution of filaments in column density. Only a small fraction of the FIR structures can be traced in H I column densities.

Matching FIR filaments with 1 km s^{-1} broad eigenvalue maps in H I visually is an even more complex task if PPV channel maps are used. Trying to find individual FIR structures within these H I maps in Fig. 9 is like looking for needles in a haystack. The H I distribution is full of filaments. Only a small fraction of these filaments are clearly linked to the FIR. Considering FIR filaments as flux tubes, the filament curvature changes across the tube envelopes (see Sect. 5 of Paper I). Increased curvatures outside the filament centers imply increased curling of magnetic field lines with decreasing field strengths as predicted for the small-scale dynamo.

Comparing the individual maps in Fig. 9 with the FIR and PPV_{fil} in Fig. 8 demonstrates impressively the power of the Hessian operator as a search algorithm for structures if both eigenvalues and eigenvectors (hence orientation angles) are used to match the data. The implication is that H I orientation angles are strongly velocity dependent. Tracing FIR in θ recovers the velocity structure of H I caustics that remain otherwise hidden in velocity slices (channel maps in PPV).

7.6. Velocity gradients for caustics in PPV and PPV_{fil}

Using caustics in PPV in place of PPV_{fil} databases has significant consequences for the determination of velocity gradients. As pointed out by Burkhardt (2021), MHD theories predict that velocity fluctuations trace magnetic field fluctuations around turbulent eddies. It is expected that the amplitude of velocity gradi-

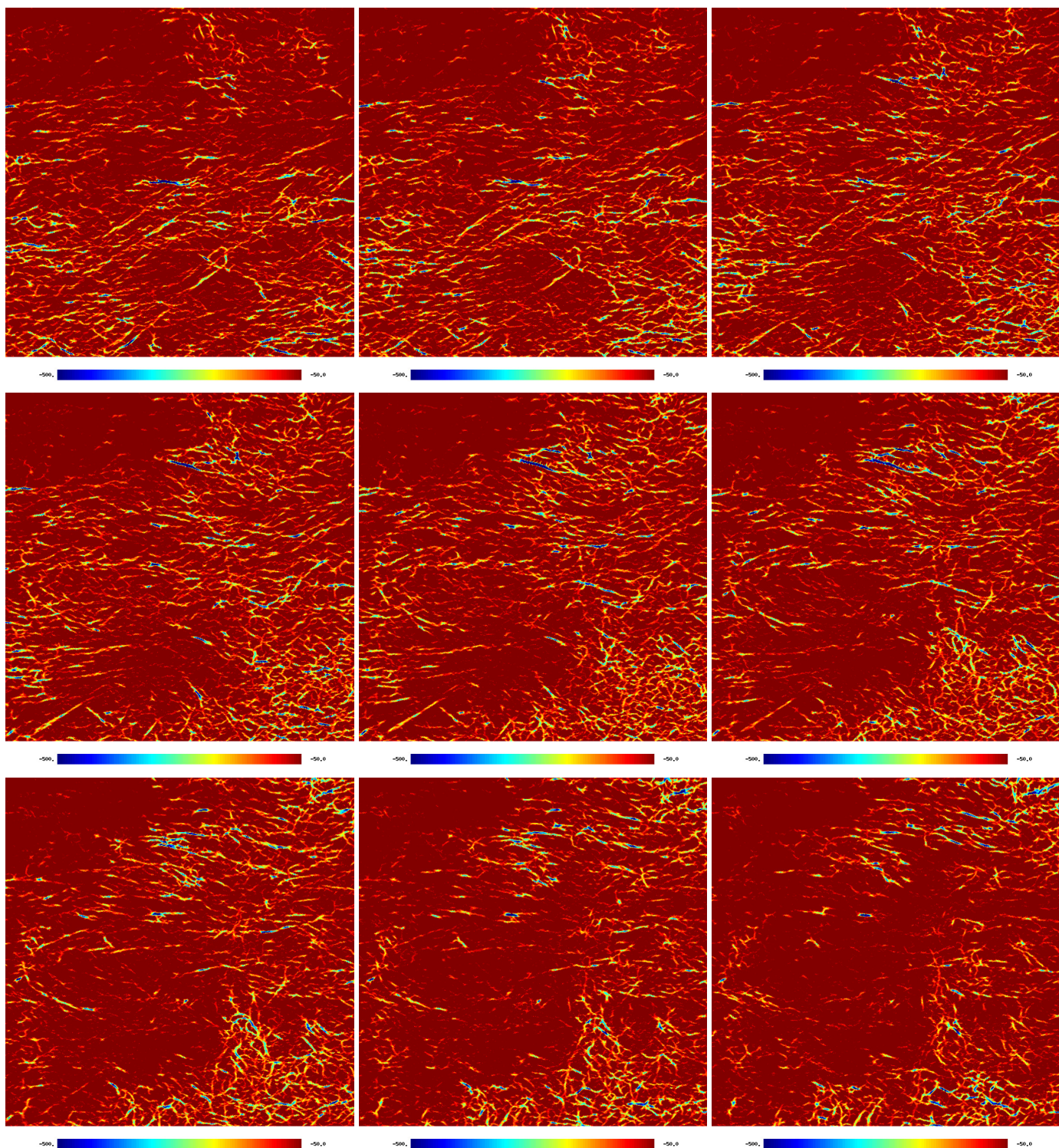


Fig. 9. PPV maps of filamentary structures at $l = 160^\circ$, $b = 30^\circ$ in gnomonic projection. The coordinates are identical to those in Fig. 2. Shown are H1 eigenvalues $\lambda_$ for p in channel maps with a 1 km s^{-1} channel width at velocities from -4 km s^{-1} (top left) to 4 km s^{-1} (bottom right).

ents across these eddies should increase with decreasing spatial scale. Thus, velocity gradients are expected as a tracer of magnetic fields on small scales.

The velocity gradient technique (VGT) was first applied by [González-Casanova & Lazarian \(2017\)](#) to PPV data from an isothermal medium. Since then, several publications used VGT with some modifications, we refer to the detailed discussions in [Hu et al. \(2023\)](#). VGT needs to measure gradients in PPV

maps from velocity centroids or alternatively from gradient angle maps by averaging over blocks with sizes around 100×100 pixels ([Lazarian & Yuen 2018](#)). This implies some smoothing. More importantly, VGT does not use caustics to determine velocity gradients.

For the application of the Hessian operator only a 5×5 pixel kernel is required. Caustics can be used then in a very simple way to derive velocity gradients on small scales with an average

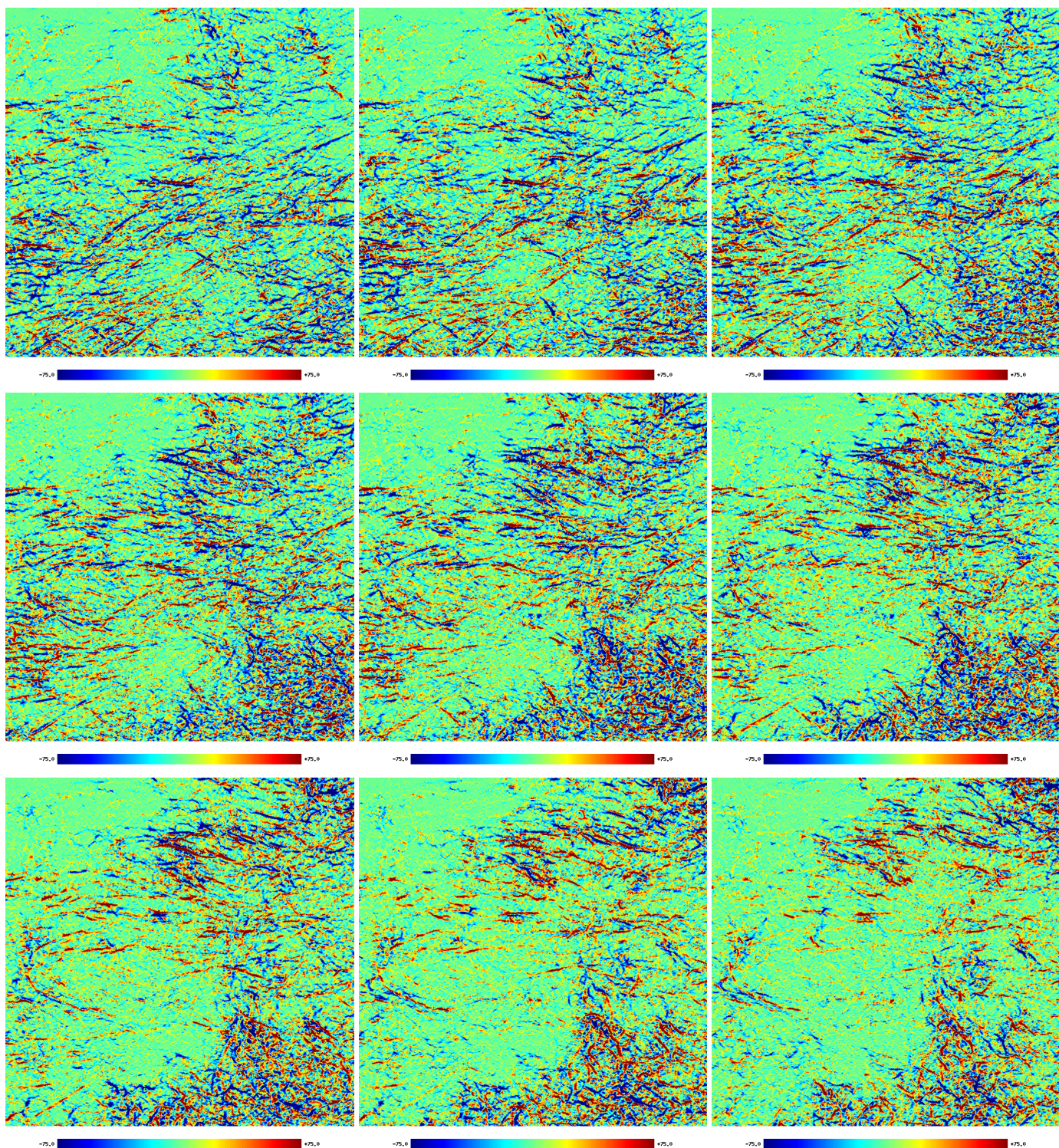


Fig. 10. PPV velocity gradient maps according to Eq. (10) for the same velocity channels displayed in Fig. 9.

filament width of 0.63 pc at a distance of 250 pc for HI4PI data. We define

$$\frac{\partial \lambda_{-}(l, b, v_{\text{LSR}})}{\partial v_{\text{LSR}}} = \frac{\lambda_{-}(l, b, v_{\text{LSR}} + \delta v_{\text{LSR}}) - \lambda_{-}(l, b, v_{\text{LSR}} - \delta v_{\text{LSR}})}{2 \delta v_{\text{LSR}}}, \quad (10)$$

and use the observational available channel width of $\delta v_{\text{LSR}} = 1 \text{ km s}^{-1}$. Figure 10 shows PPV gradient maps for the same channels that are shown in Fig. 9. Comparing the two figures, it is

obvious that velocity gradients are small-scale structures, running strictly parallel to the filament ridges.

Applying this gradient technique to the PPV_{fil} database needs the modification

$$\frac{\partial \lambda_{-}(l, b, v_{\text{fil}})}{\partial v_{\text{fil}}} = \frac{\lambda_{-}(l, b, v_{\text{fil}} + \delta v_{\text{LSR}}) - \lambda_{-}(l, b, v_{\text{fil}} - \delta v_{\text{LSR}})}{2 \delta v_{\text{LSR}}}. \quad (11)$$

Figure 11 shows the result. The differences between Figs. 10 and 11 are striking, but are readily explained in the context of

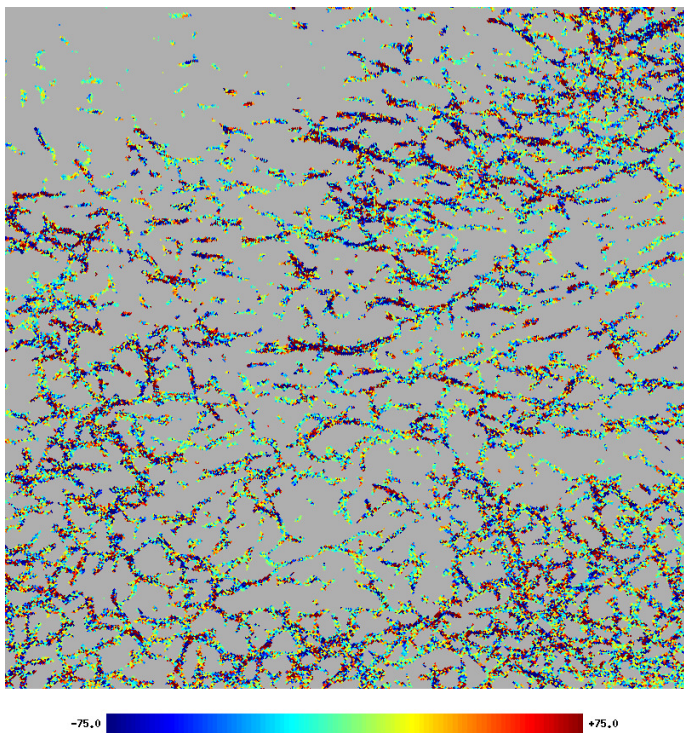


Fig. 11. PPV_{fil} velocity gradient map according to Eq. (11) for comparison with Fig. 10.

caustics as descending manifolds. $H\text{I}$ filaments represent passes with a narrow width in velocity space. PPV_{fil} filaments are located on top of the passes. The Morse lemma tells us that for smooth functions of variables with a nondegenerate critical point at the origin there exists a local diffeomorphism that preserves the origin and approximates the original function with a quadratic function (e.g., [Castrigiano & Hayes 2004](#)). Thus, on top of a saddle it is flat, and gradients are low. Figure 11 shows essentially only noise, but no systematic gradients. As soon as we get to the wings of the descending manifold, gradients may get steep. Backpackers, walking on passes, know this rule by experience. Steep gradients with narrow filamentary structures in Fig. 10 come from the fact that filaments in Fig. 9 are made of CNM, and hence they all have narrow line widths, typically $\Delta v_{\text{LSR}} = 3 \text{ km s}^{-1}$.

The filaments in Fig. 9 and the gradients in Fig. 10 are PPV structures, and hence they represent caustics that are affected by turbulent velocity fluctuations. Orientation angles are known only for a small fraction of these structures associated with FIR filaments. Only for this restricted subset of filamentary structures (Fig. 11) is it possible to separate turbulent contribution and average filament velocities as detailed in Sect. 2.2. These common FIR/ $H\text{I}$ filaments represent prominent ridges within a network of associated $H\text{I}$ filaments.

8. Summary and conclusion

$H\text{I}$ shows for large parts of the diffuse ISM filamentary structures and it is well established that these are correlated with FIR emission and aligned with the ambient magnetic field (e.g., [Clark et al. 2014](#), [Clark et al. 2015](#) or [Kalberla et al. 2016](#)). These authors identified the structures with actual $H\text{I}$ density filaments. The interpretation of the filaments as density structures is in conflict with [Lazarian & Pogoyan \(2000\)](#). Their VCA postulate is that

turbulent velocity fluctuations along the line of sight makes emitting elements at different distances from the observer overlap in velocity space. This effect, also called velocity mapping, causes velocity caustics that are said to be dealt with from a mathematical perspective in [Arnold et al. \(1985\)](#).⁶ Thus, multiple elements along the line of sight at the same velocity cause enhanced emission in the observations that does not exist in position space ([Lazarian & Yuen 2018](#) and Fig. 1 in [Hu et al. 2023](#)).

Following VCA, a number of publications corroborated the velocity caustics model. The discussion about density structures or velocity caustics cumulated with the publications of [Lazarian & Yuen \(2018\)](#) and [Clark et al. \(2019\)](#) in an open conflict. In turn, the existence of dense structures and further the association between FIR structures and $H\text{I}$ counterparts was proven (e.g., [Clark et al. 2019](#), [Peek & Clark 2019](#), [Clark & Hensley 2019](#), [Murray et al. 2020](#), [Kalberla et al. 2020](#), Paper I, and Paper II). Filaments were found to be associated with particular cold CNM, an increased CNM fraction and an enhanced FIR emissivity $I_{\text{FIR}}/N_{\text{HI}}$.

In response, [Yuen et al. \(2021\)](#) developed a numerical model called VDA to separate velocity and density fluctuations in the VCA framework. This model was supposed to support VCA, and this presentation has been recently reinforced by [Hu et al. \(2023\)](#).

We applied the VDA model to HI4PI observations used by Paper I and Paper II. The main body of our paper is about the performance of the VDA algorithm. Summarizing our results, we note first that structures that were called velocity caustics in the literature are not caustics as defined by [Thom \(1975\)](#) and [Arnold et al. \(1985\)](#) or in the recent literature by [Sousbie \(2011\)](#), among others. VDA velocity and density data are modified data products that, in a way similar to that used for the original observations, may contain caustics. These caustics need to be determined, following the standard procedures explained by [Sousbie \(2011\)](#), [Sousbie et al. \(2011\)](#), [Feldbrugge et al. \(2018\)](#), and [Feldbrugge et al. \(2019\)](#), among others.

Since the year 2000 has become customary for a group of authors to describe and cite $H\text{I}$ structures as velocity caustics without giving any proof that they are actually caustics. In the literature there exists a clear classification of critical points and procedures for deriving caustics, and one would expect such definitions to be followed. Only a small fraction (typically 30%) of the structures visible in VCA/VDA velocity caustic maps p_v are related to generic caustics. These filamentary structures, classified as A_3 by [Arnold et al. \(1985\)](#), must be worked out before they can be called caustics, otherwise the terminology is misleading. In other words, the caustics of the velocity caustics need to be determined. In the literature, images of velocity caustics are published that do not at all show similarities to the examples of caustics from the observations given here. A few RHT images have been published by [Hu et al. \(2023\)](#), among others, but it is unclear how they are related to FIR structures.

To determine caustics, we applied the same Hessian analysis as in Paper I to the VDA data and found that caustics from VDA velocity data are almost identical with caustics from the original observations. The Pearson product-moment correlation coefficient is $\geq 98\%$. Tracing *Planck* FIR caustics at 857 GHz, we recovered 97% of the filaments from the original $H\text{I}$ database with the VDA velocity data. In the mathematical framework of caustics in smooth differentiable maps, caustics from VDA velocity data can be considered as local diffeomorphisms to the

⁶ We were unable to find a treatment of mapping effects, such as velocity crowding, in this book.

caustics from direct H I observations. Thus, the VDA decomposition algorithm does not provide any advantages. Comparing the alignment measures when fitting FIR and H I filament structures, the residual misalignment from fitting uncertainties increases in case of VDA velocity caustics. We conclude that H I filament structures cannot be significantly affected by turbulent velocity crowding, contrary to VCA/VDA predictions. The density model based on original unmodified data performs better. Filaments derived from VDA velocity caustics are correlated in the same way as caustics derived in Paper I, with caustics from broadband FIR emission. The assertion by Hu et al. (2023) that the data analysis in Paper II did not consider velocity caustics is not justified (see Kalberla et al. 2021b, with a preliminary version of Sect. 4).

In the same way as intensity fluctuations in the VDA framework can arise from both density and velocity perturbations, VCA predicts that the observed H I power distribution can be decomposed in velocity and density terms. These can be characterized with narrow and broad velocity channel data and, according to VCA, they should differ significantly from each other. We calculated VDA velocity and density power spectra. The power spectra are straight; there are no significant differences between the VDA velocity power spectrum and the spectrum from the original H I data. All spectral indices agree within the errors. There is no evidence for the VCA predicted change of the power spectrum with respect to the used velocity width, defining velocity, or density effects in VDA.

The VDA predicts significant differences between data products from the original H I data and the decomposed velocity and density terms. The result that VDA velocity data and original H I observations deliver nearly identical caustics rises the question whether the VDA decomposition is based on any physical background. One of the discussed topics is the question whether filamentary H I structures that originate from small-scale fluctuations are linked to the CNM with narrow line widths.

We considered the BIGHICAT compilation of absorption data that are available from McClure-Griffiths et al. (2023). We found that 63 out of 66 observations without detectable absorptions are located outside FIR/H I filaments, and 174 positions from the absorption survey could be used to determine absorption components within FIR/H I filaments. The derived H I spin temperatures and also the corresponding volume densities are typical for temperatures of the CNM. This is not a new result, but for the first time it has been shown that the CNM in the diffuse ISM is exclusively located in filaments with FIR counterparts. We conclude that FIR/H I filaments trace the CNM in the same way as FIR filaments trace cold dust. These caustics are density structures, consistent with previous findings (e.g., Clark et al. 2019, Peek & Clark 2019, Clark & Hensley 2019, Murray et al. 2020, Kalberla et al. 2020, Paper I, and Paper II).

The VCA and descendants, as reviewed by Burkhart (2021), relies on a PPV decomposition algorithm in the channel maps. We demonstrate in Fig. 9 that individual channels in the PPV database are not optimal for the detection and tracing of FIR filaments. In the same way, velocity gradients in PPV are hard to interpret (Fig. 10). In Paper I it was shown that the distribution of curvatures in filaments follows closely the expected curvature distribution in the case of a turbulence-driven small-scale dynamo. The filament curvature is related to the magnetic field strength (Schekochihin et al. 2004). Sharply curved fields imply a high field tension, and the field strength is reduced. For the small-scale dynamo the magnetic field amplification is exponentially fast and occurs due to stretching of the magnetic field lines by the random velocity shear associated with the turbulent eddies. According to Matthaeus et al. (2008), the local

directional alignment of the velocity and magnetic field fluctuations is expected to occur rapidly. However, these calculations missed an important term. The full expression is given by Soler & Hennebelle (2017), their MHD simulations, however, only cover densities $n \gtrsim 3000 \text{ cm}^{-3}$. Densities in our case are far below this value; we observe caustics and velocity gradients that are aligned with the magnetic field. In all cases H I column densities are below $N_H = 10^{21.7} \text{ cm}^{-2}$ and the magnetic field is expected to be aligned parallel to the filaments (Hennebelle & Inutsuka 2019).

Observed local H I orientation angles are strongly velocity dependent. This implies that H I filaments must have narrow velocity dispersions. The turbulent velocity field is expected to introduce some local filament bending. In projection, if this happens along the line of sight, the bending cannot be observed in position. However, a velocity induced bending causes changes in orientation angle. Filament tracing is therefore a tracing in position on the plane of the sky and is analogous in orientation angle for the velocity along the line of sight. Instead of a PPV alignment we need to consider a PPV_{fil} geometry, tracing the filament also in filament velocity v_{fil} . Such a tracing is provided in a natural way if the Hessian analysis uses the full information, eigenvalues, and eigenvectors (hence orientation angles) from FIR filaments. This PPV_{fil} tracing has to be done for each individual filament and v_{fil} includes position-dependent turbulent velocity fluctuations. In the case that filaments are positionally disjunct (at high Galactic latitudes only a small amount of confusion is expected; see Paper II) the v_{fil} data can be combined to a large-scale velocity field for the filaments.

The significant difference between PPV_{fil} density structures and PPV velocity crowding from the VCA theory is the distribution of matter along the line of sight. In the first case fibers are bent as density structures in PPV_{fil}, in the second case the distribution is fluffy along the line of sight because of different separate components that cause H I velocity crowding. Both approaches can only be consistent if velocity crowding exists on scales that are compatible with the radial extensions of the FIR/H I caustics. Such a solution is however explicitly ruled out by Lazarian & Yuen (2018) for longwave-dominated power spectra with a steep spectral index ($\gamma < -3$). A shortwave-dominated or shallow velocity spectrum with $\gamma \gtrsim -3$ is not considered to be physically motivated (Chepurnov & Lazarian 2009).

Our results are in conflict with such theoretical expectations. We get an average multiphase H I spectral index of $\gamma = -2.85$. According to McClure-Griffiths et al. (2023), this index is representative for the H I at high Galactic latitudes. For the CNM the power spectrum flattens to $\gamma = -2.5$ (Kalberla & Haud 2019), approaching $\gamma = -2.4$ as the spectral index of the turbulent magnetic field (Ghosh et al. 2017; Adak et al. 2020). Turbulence in FIR/H I filaments is driven on small scales by a fluctuation dynamo (Paper I), in conflict with a longwave-dominated power law, as assumed by Lazarian & Yuen (2018). Here we argue based on observational results against theoretical expectations.⁷

⁷ Hu et al. (2023, Sect. 7.3.6) found that the decomposition of H I observations by Kalberla & Haud (2020b) result in steep CNM power spectra in the case of thin channels, suggesting that small-scale CNM structures are rare in thin channels compared to those in thick channels. Our comment on this statement is the following: Single channel CNM power spectra have been shown to be flat, $\gamma \gtrsim -2.5$ (e.g., Kalberla & Haud 2019, Figs. 1, 9, 13, and 23, and Kalberla & Haud 2020b, Figs. 3–5). The assertion that small-scale CNM structures are rarer in thin channels than in thick channels is incompatible with H I observations, also with our current results. Observational conflicts with Clark et al.

Acknowledgements. We acknowledge the referee for careful reading and comments that supported an improvement of the current manuscript. We thank Naomi McClure-Griffiths and Daniel Rybarczyk for help with the BIGHICAT database. We acknowledge the referee of a previous version of this manuscript for constructive comments that helped to improve the quality of this version as a separate paper. HI4PI is based on observations with the 100-m telescope of the MPIfR (Max-Planck- Institut für Radioastronomie) at Effelsberg and the Parkes Radio Telescope, which is part of the Australia Telescope and is funded by the Commonwealth of Australia for operation as a National Facility managed by CSIRO. This research has made use of NASA's Astrophysics Data System. Some of the results in this paper have been derived using the HEALPix package.

References

- Blandford, R. D. & Narayan, R. 1992, *ARA&A*, 30, 311
 Adak, D., Ghosh, T., Boulanger, F., et al. 2020, *A&A*, 640, A100
 Arnold, V.I., Varchenko, A. & Gusein-Zade, S.M., *Singularities of Differentiable Maps: Volume I: The Classification of Critical Points Caustics and Wave Fronts*, 1985, Birkhäuser, Boston
 Bond, J. R., Kofman, L., & Pogosyan, D. 1996, *Nature*, 380, 603
 Burkert, A. 2006, *Comptes Rendus Physique*, 7, 433
 Burkhart, B. 2021, *PASP*, 133, 102001
 Castrigiano, D. & Hayes, S. 2004, *Catastrophe Theory: (2nd ed.)*, CRC Press.
 Chepurnov, A. & Lazarian, A. 2009, *ApJ*, 693, 1074
 Clark, S. E., Peek, J. E. G., & Putman, M. E. 2014, *ApJ*, 789, 82
 Clark, S. E., Hill, J. C., Peek, J. E. G., et al. 2015, *Phys. Rev. Lett.*, 115, 241302
 Clark, S. E., Peek, J. E. G., & Miville-Deschênes, M.-A. 2019, *ApJ*, 874, 171
 Clark, S. E. & Hensley, B. S. 2019, *ApJ*, 887, 136
 Esquivel, A., Lazarian, A., Pogosyan, D., et al. 2003, *MNRAS*, 342, 325
 Federrath, C. & Banerjee, S. 2015, *MNRAS*, 448, 3297
 Feldbrugge, J., van de Weygaert, R., Hidding, J., et al. 2018, *J. Cosmology Astropart. Phys.*, 2018, 027
 Feldbrugge, J., van Engelen, M., van de Weygaert, R., et al. 2019, *J. Cosmology Astropart. Phys.*, 2019, 052
 Feldbrugge, J. & van de Weygaert, R. 2023, *J. Cosmology Astropart. Phys.*, 2023, 058
 Ghosh, T., Boulanger, F., Martin, P. G., et al. 2017, *A&A*, 601, A71
 González-Casanova, D. F. & Lazarian, A. 2017, *ApJ*, 835, 41
 Heiles, C. & Troland, T. H. 2005, *ApJ*, 624, 773
 Heiles, C. & Haverkorn, M. 2012, *Space Sci. Rev.*, 166, 293
 Hennebelle, P. & Inutsuka, S.-. ichiro . 2019, *Frontiers in Astronomy and Space Sciences*, 6, 5
 HI4PI Collaboration, Ben Bekhti, N., Flöer, L., et al. 2016, *A&A*, 594, A116
 Ho, K. W. & Lazarian, A. 2023, *MNRAS*, 520, 3857
 Hu, Y., Lazarian, A., Alina, D., et al. 2023, *MNRAS*, 524, 2994
 Hu, Y. & Lazarian, A. 2023, *MNRAS*, 524, 2379
 Jenkins, E. B. & Tripp, T. M. 2011, *ApJ*, 734, 65
 Jow, D. L., Hill, R., Scott, D., et al. 2018, *MNRAS*, 474, 1018
 Kalberla, P. M. W. & Haud, U. 2015, *A&A*, 578, A78
 Kalberla, P. M. W., Kerp, J., Haud, U., et al. 2016, *ApJ*, 821, 117
 Kalberla, P. M. W. & Haud, U. 2019, *A&A*, 627, A112
 Kalberla, P. M. W., Kerp, J., & Haud, U. 2020, *A&A*, 639, A26
 Kalberla, P. M. W. & Haud, U. 2020b, arXiv:2003.01454
 Kalberla, P. M. W., Kerp, J., & Haud, U. 2021, *A&A*, 654, A91
 Kalberla, P. M. W., Kerp, J., & Haud, U. 2021b, arXiv:2101.00273
 Kalberla, P. M. W. & Haud, U. 2023, *A&A*, 673, A101
 Kandel, D., Lazarian, A., & Pogosyan, D. 2016, *MNRAS*, 461, 1227
 Koch, E. W. & Rosolowsky, E. W. 2015, *MNRAS*, 452, 3435
 Lazarian, A. & Pogosyan, D. 2000, *ApJ*, 537, 720
 Lazarian, A. & Pogosyan, D. 2004, *ApJ*, 616, 943
 Lazarian, A. & Pogosyan, D. 2006, *ApJ*, 652, 1348
 Lazarian, A. & Pogosyan, D. 2008, *ApJ*, 686, 350
 Lazarian, A. & Yuen, K. H. 2018, *ApJ*, 853, 96
 Mattheaus, W. H., Pouquet, A., Mininni, P. D., et al. 2008, *Phys. Rev. Lett.*, 100, 085003
 McClure-Griffiths, N. M., Stanimirović, S., & Rybarczyk, D. R. 2023, *ARA&A*, 61, 19
 Mittal, A. K., Babler, B. L., Stanimirović, S., et al. 2023, *ApJ*, 958, 192
 Murray, C. E., Peek, J. E. G., & Kim, C.-G. 2020, *ApJ*, 899, 15
 Padoan, P., Juvela, M., Kritsuk, A., et al. 2009, *ApJ*, 707, L153
 Peek, J. E. G. & Clark, S. E. 2019, *ApJ*, 886, L13
 Planck intermediate results XXXII. 2016, *A&A*, 586, A135
 Planck intermediate results XXXV, Ade, P. A. R., Aghanim, N., et al. 2016, *A&A*, 586, A138
 Planck intermediate results XXXVIII, Ade, P. A. R., Aghanim, N., et al. 2016, *A&A*, 586, A141
 Planck intermediate results XLIV, Aghanim, N., Alves, M. I. R., et al. 2016, *A&A*, 596, A105
 Planck intermediate results. LVII. 2020, *A&A*, 643, A42
 Polychroni, D., Schisano, E., Elia, D., et al. 2013, *ApJ*, 777, L33
 Schekochihin, A. A., Cowley, S. C., Taylor, S. F., et al. 2004, *ApJ*, 612, 276
 Schisano, E., Rygl, K. L. J., Molinari, S., et al. 2014, *ApJ*, 791, 27
 Soler, J. D. & Hennebelle, P. 2017, *A&A*, 607, A2
 Soler, J. D., Beuther, H., Syed, J., et al. 2020, *A&A*, 642, A163
 Soler, J. D., Miville-Deschênes, M.-A., Molinari, S., et al. 2022, *A&A*, 662, A96
 Sousbie, T. 2011, *MNRAS*, 414, 350
 Sousbie, T., Pichon, C., & Kawahara, H. 2011, *MNRAS*, 414, 384
 St-Onge, D. A. & Kunz, M. W. 2018, *ApJ*, 863, L25
 Thom, R. 1975, *Structural Stability and Morphogenesis*. Benjamin-Addison-Wesley, New York.
 Winkel, B., Kerp, J., Flöer, L., et al. 2016, *A&A*, 585, A41
 Wolfire, M. G., McKee, C. F., Hollenbach, D., et al. 2003, *ApJ*, 587, 278
 Xu, S. & Lazarian, A. 2017, *New Journal of Physics*, 19, 065005
 Yuen, K. H. & Lazarian, A. 2017, *ApJ*, 837, L24
 Yuen, K. H., Ho, K. W., & Lazarian, A. 2021, *ApJ*, 910, 161

(2019) that might support VCA as reported by Hu et al. (2023) in their Sect. 7.3.6 do not exist.